

Kinetostatics and Particle-Swarm Optimization of Vehicle-Mounted Underactuated Metamorphic Loading Manipulators

Nan Mao^{a,b}, Guanglu Jia^{a, c, *}, Junpeng Chen^a, Emmanouil Spyarakos-Papastavridis^b, Jian S. Dai^{a,b,*}

^aShenzhen Key Laboratory of Intelligent Robotics and Flexible Manufacturing Systems, Institute for Robotics, Southern University of Science and Technology, Shenzhen, 518055, China

^bCentre for Robotics Research, King's College London, London, WC2R 2LS, United Kingdom

^cDepartment of Mechanical Engineering, National University of Singapore, Singapore, 119077, Singapore

* Corresponding author

E-mail: g.jia@nus.edu.sg (Guanglu Jia), jian.dai@kcl.ac.uk (Jian S. Dai)

Abstract

Fixed-degree-of-freedom (DoF) loading mechanisms often suffer from excessive actuators, complex control, and limited adaptability to dynamic tasks. This study proposes an innovative underactuated metamorphic loading manipulator, integrating a metamorphic arm and a passively adaptive gripper. The metamorphic arm employs geometric constraints, enabling topology reconfiguration and flexible motion trajectories without additional actuators. The adaptive gripper, driven entirely by the arm, accommodates diverse objects through passive compliance. Then, a structural model of the manipulator is developed, and kinematic analysis explores its isomorphic states during grasping operations. To optimize performance, particle swarm optimization (PSO) is utilized to refine the size parameters of the gripper's structure, ensuring robust adaptability across various applications. Simulation results validate the manipulator's simplified control strategy, operational versatility, and effectiveness in grasping diverse objects in dynamic environments. This work underscores the practical potential of underactuated metamorphic mechanisms in applications requiring efficient and adaptable loading solutions.

Keywords: kinematic analysis; metamorphic manipulator; underactuated mechanism; mechanism synthesis; parameter optimization

1. Introduction

With the increasing integration of robotics across various sectors, including industrial production and daily life, the demand for advanced robotic grasping capabilities has grown significantly. Robotic hands, emulating the fundamental functions of the human hand, are extensively utilized across various domains such as aerospace and manufacturing [1]. These hands are typically mounted at the terminus of a mechanical arm, known as the end-effector, and have been the focus of substantial research over the past three decades. The development of robotic hands has seen remarkable progress, with many scholars contributing significantly to the field [2], including the Utah/MIT hand [3], TUAT/Karlsruhe hand [4], and BCL-13 [5].

However, traditional manipulators face challenges due to their numerous actuation components, intricate control systems, and limited adaptability, making it hard to reconcile the trade-offs among a simple structure, a large grasping force, flexibility [6], and the ability to grasp objects automatically adaptively [7]. To address these challenges, flexible manipulators are characterized by high dexterity, light weight, and low stiffness, attracting scholars from various countries to conduct extensive research [8]. Typical flexible manipulators are exemplified by the flexible humanoid hand developed by Ohio State University in the United States [9], the Octopus Gripper produced by Festo in Germany [10], and the three-finger pneumatic soft manipulator created by Ritsumeikan University in Japan [11]. In China, typical soft manipulators consist of the pneumatic soft manipulator from Shanghai Jiao Tong University [12], the four-finger soft manipulator of Beihang University [13], and the two-finger soft manipulator from National Cheng Kung University in Taiwan, China [14].

In the realm of robotic manipulators, the challenge of excessive weight and cost is pronounced due to the need for individual actuators to power each joint's degree of freedom, along with sophisticated control and sensing systems [15]. These limitations have motivated the pursuit of manipulators that can perform complex grasping tasks with simplified control and reduced weight [16], leading to the development of underactuated robotic fingers, such as the SDM [17], PASA-GB hand [18], and SARAH [19-22]. Underactuated manipulators, which require fewer actuators than degrees of freedom [23], utilize a hybrid actuation strategy that combines active motors with passive elements like springs or coupling mechanisms to achieve grasping capabilities [24]. This design enables the underactuated hand to perform multi-tiered grasping actions [25], adaptively handling items of various shapes and sizes [26]. In unstructured environments, the adaptability of robotic hands is crucial for efficient grasping and manipulation, prompting the innovation of metamorphic robotic hands [27, 28], marking a significant advancement in the dexterity and functionality of robotic hands.

Metamorphic mechanisms have the characteristics of variable mobility and topology [29, 30]. They can self-assemble and reconfigure [31], changing their configuration during operation [32], adapting the loading manipulator to the task requirements of different work stages, and maximizing its functionality [33]. Originating from biological terminology, 'metamorphosis' describes the process of transformation and structural adaptation [34]. Applied to robotics, Dai introduced the concept of the metamorphic mechanism in 1998 [35, 36]. Subsequently, mechanisms are reconfigurable [37], enabling variable mobility and topology for the robots during operation [38], which greatly enhances their functionality and adaptability [39]. Furthermore, a methodology for synthesis and configuration design of metamorphic mechanisms has been developed [40]. Building on these concepts, a range of metamorphic mechanisms have been introduced, encompassing those with adjustable topologies [41] and multi-modal capabilities [42] such as the origami-inspired integrated 8R kinematotropic metamorphic mechanism [43]. This design incorporates mathematical and topological insights [44] to achieve greater dexterity [45].

Combining the advantages of the underactuated principle and metamorphic mechanism, this study creates a novel underactuated metamorphic loading manipulator that features a streamlined design and enhanced versatility.

Particle swarm optimization (PSO) is one of the most well-regarded swarm-based algorithms [46] introduced by Kennedy and Eberhart [47], has been applied in a host of areas such as mechanism optimization [48], parameter selection, and topology structure [49, 50]. In recent years, robotics has witnessed significant adoption of intelligent PSO algorithms for parameter optimization [51]. Gong et al. [52] developed a hybrid optimization algorithm combining bee swarm and PSO to optimize manipulator parameters. Wang et al. [53] introduced a universal index with an enhanced PSO for precise pose selection. Fang and Dang [54] presented a QPSO method for kinematic calibration across serial and parallel robots, enhancing calibration accuracy. These contributions underscore the evolving landscape of parameter identification in robotics [55].

This research presents a study and discussion on the kinematic and contact force analysis, and parameter optimization using the PSO Algorithm, determining the best parameters of the underactuated metamorphic loading manipulator. The validity of the established model is verified through Simulation. The main contributions of this paper are as follows:

- (1) We design an underactuated metamorphic system driven by a sole motor. This system can complete all tasks such as grasping, releasing, lifting, and descending, facilitating adaptive metamorphic grasping of differently shaped objects.
- (2) Through kinematic and contact force analysis of the manipulator, we can determine the length of each finger joint based on the dimensions of the target object, enabling the manipulation system to evolve into a series of products for practical applications.
- (3) We have engineered the best optimized structure of the manipulator by developing the PSO algorithm to refine the gripper's structural parameters. This approach ensures that, under constrained driving forces, the force is distributed evenly across the finger joints, thereby optimizing the gripping strength.

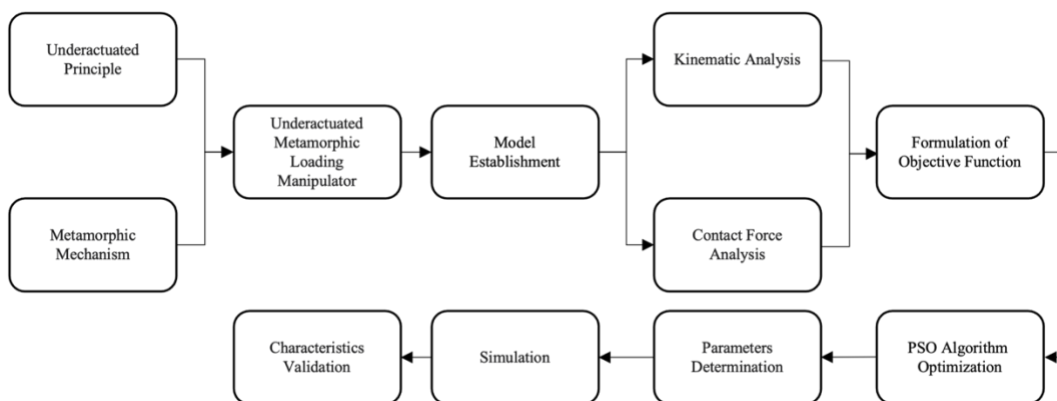


Figure 1. Flow diagram of the underactuated metamorphic loading manipulator.

The flowchart presented in **Figure 1** provides a comprehensive overview of the design methodology for the underactuated metamorphic loading manipulator as proposed in this paper. The process is systematic and iterative, ensuring that each stage builds upon the previous one to achieve an optimal design. We developed an underactuated metamorphic robotic manipulator, detailing its metamorphic mechanism and underactuated principle to enhance adaptability. A mathematical model was constructed to capture the manipulator's dynamics and kinematics, forming the basis for subsequent analyses. Kinematic analysis across various motion modes was conducted to optimize task adaptation and transition smoothness. Contact force distribution on the gripper was analyzed using static models and virtual work principles, which are crucial for manipulator stability and performance. An objective function for gripper performance was formulated, focusing on uniform contact force distribution, with design variables identified for optimization. The Particle Swarm Optimization (PSO) algorithm was utilized to refine the gripper's structural parameters, addressing complex, nonlinear, multidimensional optimization challenges. Finally, simulation validated the manipulator's performance in grasping objects of diverse sizes and shapes. This systematic approach ensures the manipulator's theoretical robustness and practical optimization, positioning it as a significant contribution to robotics and automation.

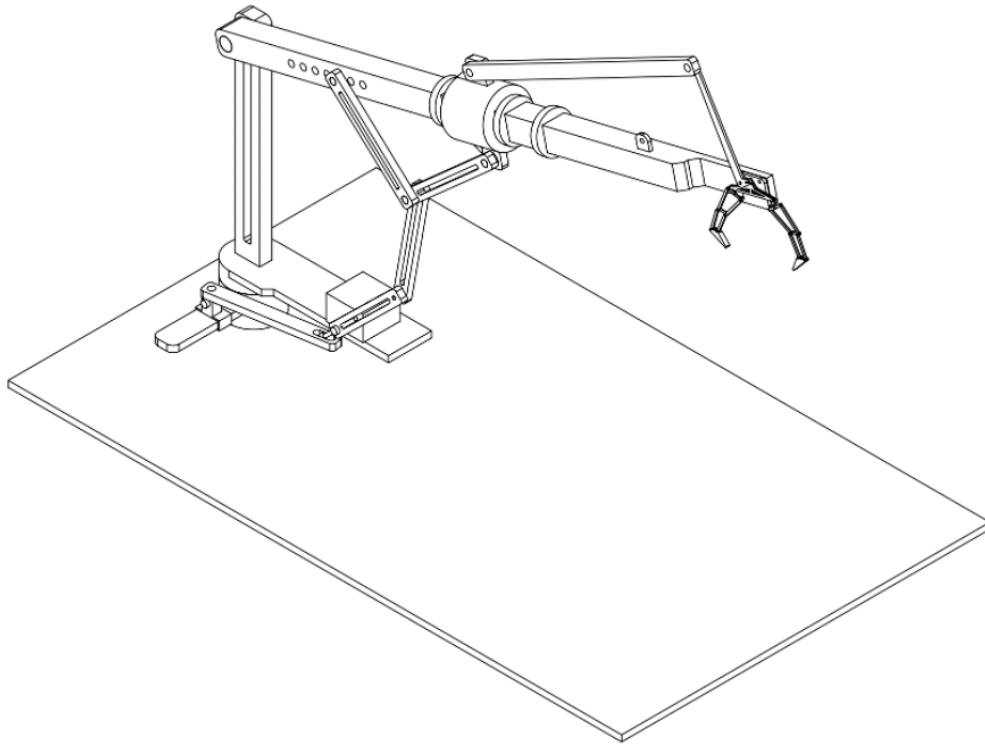
The remainder of this paper is organized as follows. Following the introduction, Section 2 outlines the overall structural model of the underactuated metamorphic loading manipulator, and examines the various isomorphic configurations of the manipulator's fingers during object grasping. In Section 3, we conduct kinematic analysis of the manipulator. Then, the finger's structural parameters have been meticulously adjusted to generate ample gripping force, ensuring steadfast control over objects even with a restricted actuation capacity. Furthermore, to promote a more consistent distribution of contact forces among the fingers and the grasped object, a Particle Swarm Optimization (PSO) algorithm is utilized to refine the gripper's parameter settings in Section 4. Section 5 involves a simulation model of the underactuated manipulator grasping tests using objects of varying sizes and shapes to validate the proposed strategies, followed by an analysis of the simulation results. Lastly, the conclusion is presented in Section 6.

2. Model of the Underactuated Metamorphic Loading Manipulator

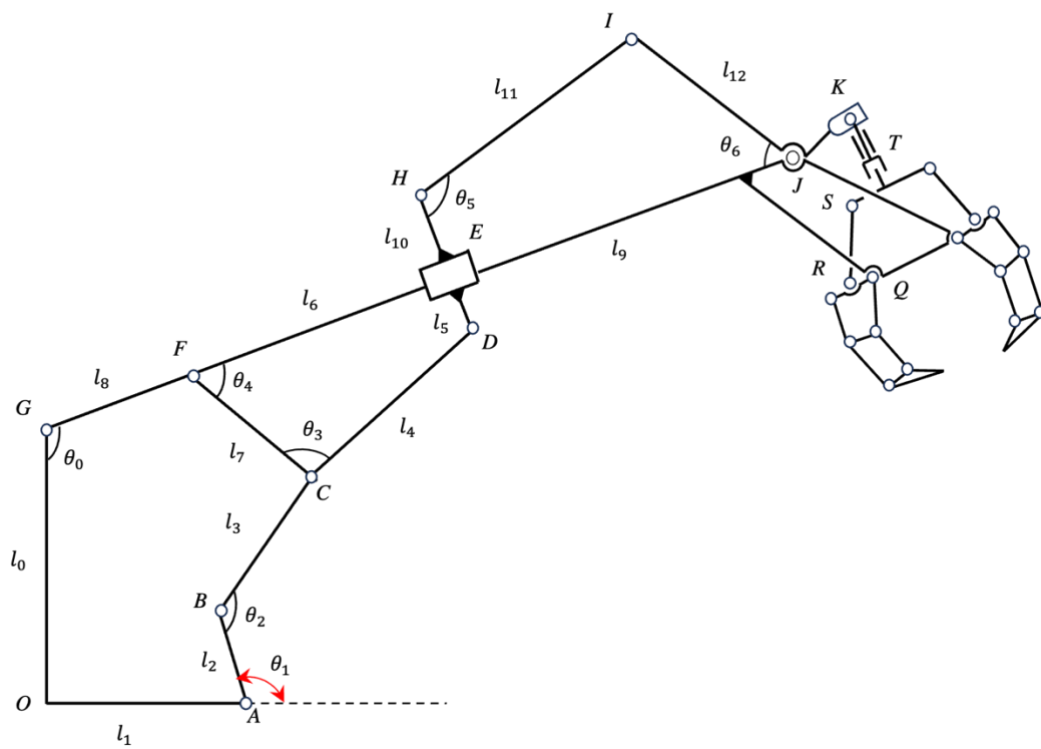
In this groundbreaking study, we introduce an avant-garde manipulator that stands out for its compact design, user-friendly control mechanisms, and exceptional adaptability. Our underactuated metamorphic loading manipulator is a marvel of modern engineering, designed to harness the power of both active and passive driving forces through the use of a single motor. This dual-drive capability enables the manipulator to dynamically interact with objects of diverse geometries, adaptively grasping and releasing them with precision and ease.

One of the key innovations of this manipulator is its ability to alter its configuration by merging or separating its components. This metamorphic quality allows the manipulator to adjust the number of active elements and modify its topological structure on-the-fly, ensuring that it can seamlessly adapt to the varying requirements of different operational stages. This adaptability is crucial for maximizing the manipulator's functionality and ensuring that it remains a versatile tool across a wide range of applications.

The intricate yet elegant design of the Underactuated Metamorphic Loading Manipulator is vividly depicted in **Figure 2**, which provides a comprehensive overview of the manipulator's structure. This figure is instrumental in illustrating the innovative aspects of our design, showcasing how each component contributes to the overall performance and adaptability of the manipulator. The figure serves as a visual testament to the manipulator's potential to revolutionize the field of robotics and automation, offering a glimpse into the future of smart, adaptable robotic systems.



(a)



(b)

Figure 2. General assembly drawing of the manipulator.

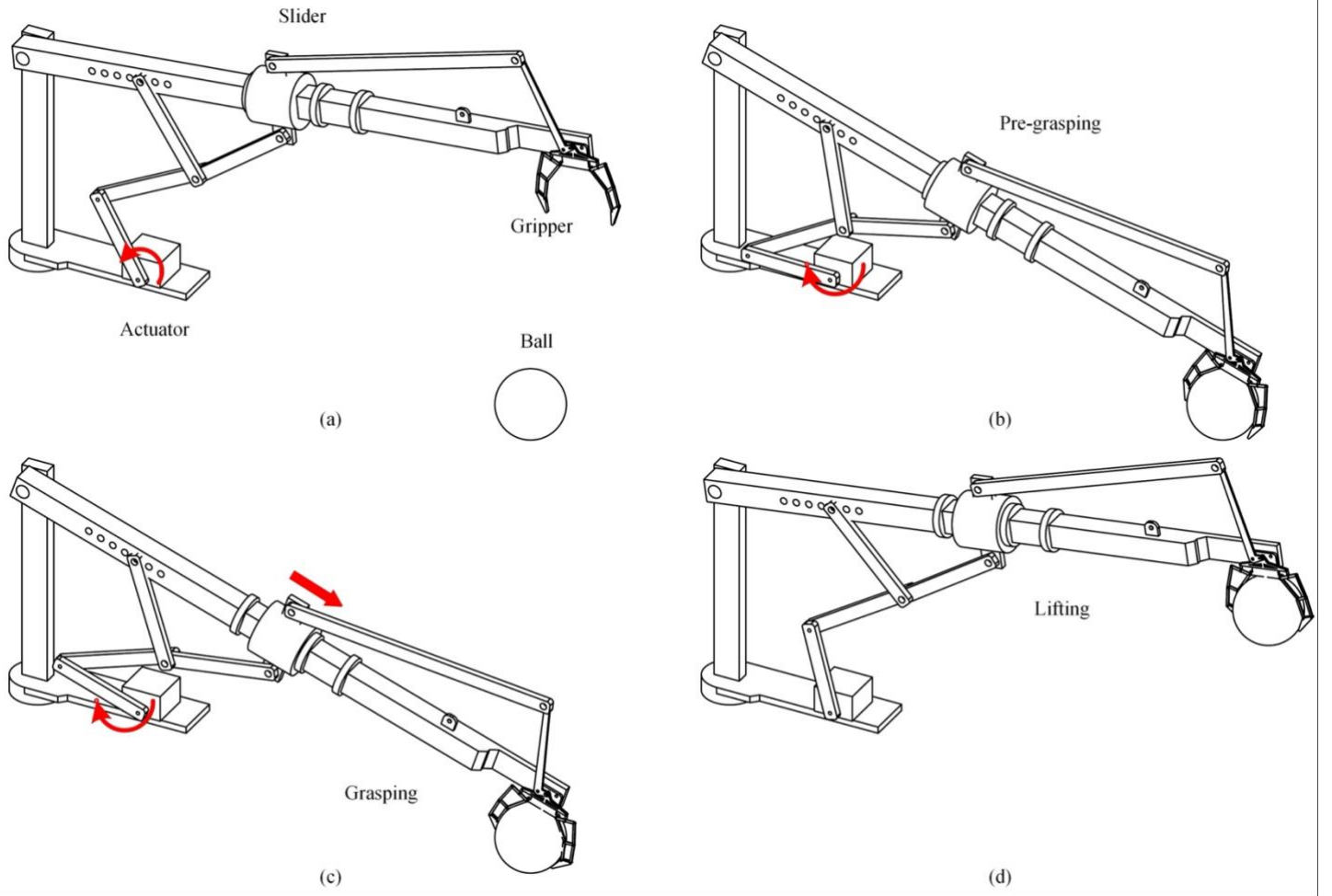


Figure 3. The process of adaptive grasping of the manipulator.

Figure 3 illustrates the grasping process of the entire metamorphic robotic arm. The metamorphic robotic arm has two configurations. When the slider is restrained by the limit block, the actuator can make the entire robotic arm perform lifting and lowering movements, as shown in **Figures 3(a)** and **3(d)**. When the slider is released, the lateral movement of the slider can control the opening and closing of the adaptive gripper, as shown in **Figures 3(b)** and **3(c)**. The topological change of the robotic arm is achieved through the geometric limitation of the slider. Meanwhile, the adaptive gripper, as an underactuated mechanism, can adapt to grasp different objects. The grasping process is as follows: **Figures 3(a)** represents the initial posture of the robotic arm. At this moment, the actuator rotates counterclockwise, and the end effector of the robotic arm lowers to approach the object to be grasped. When the robotic arm reaches **Figures 3(b)**, it is in the pre-grasping state; when the actuator rotates clockwise, the gripper closes to complete the adaptive grasping, as shown in **Figures 3(c)**; as the actuator continues to rotate clockwise and the slider reaches the limit, the robotic arm completes the grasp and lifting, as shown in **Figures 3(d)**. Thus, adaptive grasping and picking are achieved with only one actuator.

3. Kinematics and Contact Force Analysis of Underactuated Metamorphic Loading Manipulator

In this segment of our scientific investigation, we posit a critical assumption that the gripper section of our robotic manipulator receives an input force that is perpendicular to the upper arm through the intermediary of a slider mechanism. This assumption is pivotal as it allows us to decouple the complex dynamics of the gripper from the broader analysis of the robotic arm, thereby facilitating a more focused and detailed examination of each component's behavior.

The decoupling of the gripper analysis is not merely a theoretical convenience; it is a strategic approach that enables us to isolate the forces and movements acting upon the gripper, which is crucial for understanding its performance and optimizing its design. By separating the gripper's dynamics from those of the arm, we can more accurately model the gripper's response to various operational conditions and refine its control algorithms accordingly.

Our subsequent analysis will delve into the intricate relationship between the slider and the vertical input force exerted on the gripper. This relationship is of paramount importance, as it directly influences the gripper's ability to securely grasp and manipulate objects with precision. We will scrutinize how the slider's position and movement correlate with the vertical input, and how these factors contribute to the overall performance of the gripper.

Through this detailed analysis, we aim to uncover the underlying principles governing the interaction between the slider and the gripper, and how these principles can be harnessed to enhance the manipulator's functionality. This exploration will involve a combination of theoretical modeling, computational simulations, and simulation testing, all of which are essential for validating our assumptions and refining our understanding of the system's behavior.

In summary, the assumption of perpendicular input to the gripper through the slider is a cornerstone of our study, allowing us to dissect the complex interactions within the robotic manipulator and to optimize its design for enhanced performance in various applications. The forthcoming analysis will shed light on the nuances of this relationship, providing valuable insights that can inform the development of more advanced robotic systems.

3.1 Mechanical Arm Analysis of the Underactuated Metamorphic Loading Manipulator

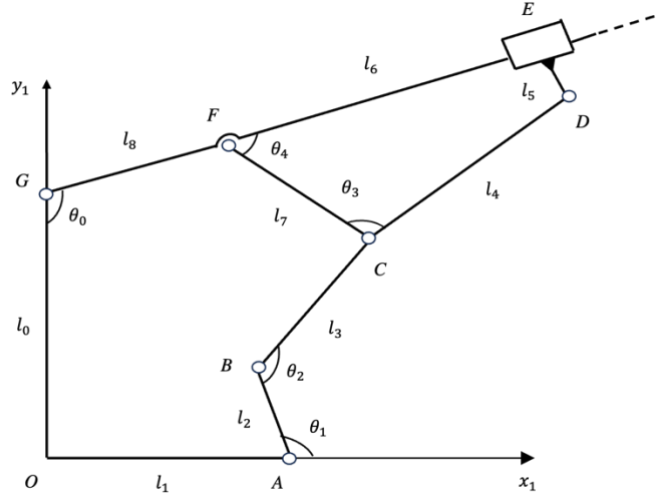


Figure 4. Schematic diagram of the equivalent mechanism of the robotic arm.

The structure of the robotic arm is illustrated in **Figure 4**. It consists of six rods and one slider. DE represents the slider, which moves freely along the upper arm GE . Points A , B , C , D , F and G are revolute joints. The system's torque input is applied at point A .

l_i represents the rod length, $i = 0, 1, 2, \dots, 8$. θ_0 represents the angle between the arm GE and vertical rod GO , θ_1 represents the angle of the drive, θ_2 represents the angle between rod 2 and 3, θ_4 represents the angle between rod 6 and 7, ω_i and β_i represents corresponding angular velocity and angular acceleration. It is assumed that throughout the operation of the robotic arm, the arm maintains a constant speed, such that $\omega_1 \neq 1, \beta_1 = 0$.

First, a positional analysis is conducted. A Cartesian coordinate system O_{xy} is established, with the origin at point O and the x -axis aligned with the direction of OA . The closed vector equation is formulated as follows:

$$\mathbf{l}_{AB} + \mathbf{l}_{BC} + \mathbf{l}_{CF} = \mathbf{l}_{AO} + \mathbf{l}_{OG} + \mathbf{l}_{GF} \quad (1)$$

The closed vector equation is projected onto the x and y directions, yielding the position equations as follows:

$$\begin{aligned} x: \quad & l_2 \cos \theta_1 - l_3 \cos(\theta_1 + \theta_2) - l_7 \sin(\theta_0 - \theta_4) = -l_1 + l_8 \sin \theta_0 \\ y: \quad & l_2 \sin \theta_1 - l_3 \sin(\theta_1 + \theta_2) + l_7 \cos(\theta_0 - \theta_4) = l_0 - l_8 \cos \theta_0 \end{aligned} \quad (2)$$

Based on the above analysis, the relationships among θ_0 , θ_1 and θ_4 under the existing dimensional parameters are illustrated in **Figure 5**.

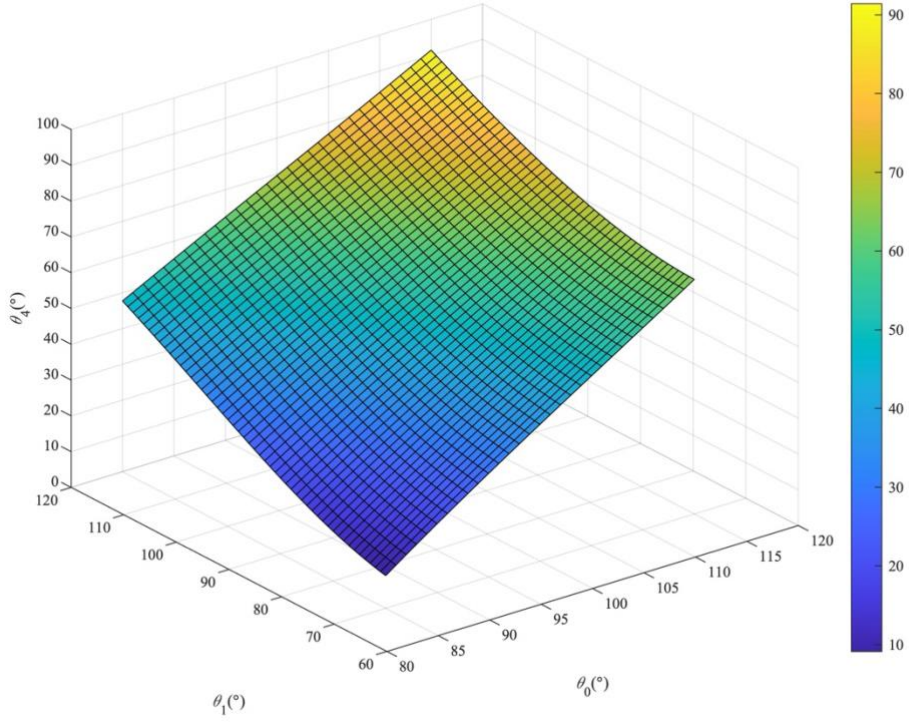


Figure 5. Relationship among θ_0, θ_1 and θ_4 .

The above equations form a nonlinear system of equations.

3.1.1 Lifting process and grasping process analysis

By fixing θ_0 and θ_4 , the motion of the robotic arm can be categorized into two processes: the lifting process and the grasping process.

During the lifting process, given θ_1 and θ_4 , the angles θ_0 and θ_2 can be determined through geometric relationships. By differentiating these relationships, the velocity expressions are obtained as follows:

$$\begin{bmatrix} l_7 \cos(\theta_0 - \theta_4) + l_8 \cos \theta_0 & -l_3 \sin(\theta_1 + \theta_2) \\ l_7 \sin(\theta_0 - \theta_4) + l_8 \sin \theta_0 & l_3 \cos(\theta_1 + \theta_2) \end{bmatrix} \begin{bmatrix} \omega_0 \\ \omega_2 \end{bmatrix} = \begin{bmatrix} -l_2 \sin \theta_1 + l_3 \sin(\theta_1 + \theta_2) \\ l_2 \cos \theta_1 - l_3 \cos(\theta_1 + \theta_2) \end{bmatrix} \omega_1 \quad (3)$$

During the grasping process, given θ_0 and θ_1 , the angles θ_2 and θ_4 can be determined through geometric relationships. By differentiating these relationships, the velocity expressions are obtained as follows:

$$\begin{bmatrix} -l_3 \sin(\theta_1 + \theta_2) & -l_7 \cos(\theta_0 - \theta_4) \\ l_3 \cos(\theta_1 + \theta_2) & -l_7 \sin(\theta_0 - \theta_4) \end{bmatrix} \begin{bmatrix} \omega_2 \\ \omega_4 \end{bmatrix} = \begin{bmatrix} -l_2 \sin \theta_1 + l_3 \sin(\theta_1 + \theta_2) \\ l_2 \cos \theta_1 - l_3 \cos(\theta_1 + \theta_2) \end{bmatrix} \omega_1 \quad (4)$$

Substituting the obtained angles yields the angular velocity of the linkage system. By differentiating again, the acceleration relationships are obtained as follows:

$$\begin{aligned}
& \begin{bmatrix} -l_3 \sin(\theta_1 + \theta_2) & -l_7 \cos(\theta_0 - \theta_4) \\ l_3 \cos(\theta_1 + \theta_2) & -l_7 \sin(\theta_0 - \theta_4) \end{bmatrix} \begin{bmatrix} \beta_2 \\ \beta_4 \end{bmatrix} \\
&= \begin{bmatrix} -l_2 \omega_1 \cos \theta_1 + l_3 (\omega_1 + \omega_2) \sin(\theta_1 + \theta_2) \\ -l_2 \omega_1 \sin \theta_1 - l_3 (\omega_1 + \omega_2) \cos(\theta_1 + \theta_2) \end{bmatrix} \omega_1 \\
&- \begin{bmatrix} -l_3 (\omega_1 + \omega_2) \cos(\theta_1 + \theta_2) & -l_7 \omega_4 \sin(\theta_0 - \theta_4) \\ -l_3 (\omega_1 + \omega_2) \sin(\theta_1 + \theta_2) & l_7 \omega_4 \cos(\theta_0 - \theta_4) \end{bmatrix} \begin{bmatrix} \omega_2 \\ \omega_4 \end{bmatrix}
\end{aligned} \tag{5}$$

Substituting the obtained angles and angular velocities yields the angular acceleration of the linkage system. From the geometric relationships, the displacement of the slider is related to θ_4 as follows:

$$l_6 = l_7 \cos \theta_4 + l_4 \sin \left(\cos^{-1} \left(\frac{l_7 \sin \theta_4 - l_5}{l_4} \right) \right) \tag{6}$$

Differentiating yields the relationship between the velocity of the slider and θ_4 and ω_4 :

$$\frac{dl_6}{dt} = -l_7 \omega_4 \sin \theta_4 + \frac{(l_7 \omega_4 \cos \theta_4)(l_5 - l_7 \sin \theta_4)}{l_4} \left(\frac{1}{\sqrt{1 - \left(\frac{l_7 \sin \theta_4 - l_5}{l_4} \right)^2}} \right) \tag{7}$$

Differentiating again yields the relationship between the acceleration of the slider and θ_4 , ω_4 , and β_4 :

$$\frac{d^2 l_6}{dt^2} = -l_7 (\beta_4 \sin \theta_4 + \omega_4^2 \cos \theta_4) + \frac{c}{\sqrt{b}} \frac{l_7 (\beta_4 \cos \theta_4 - \omega_4^2 \sin \theta_4)}{l_4} - \frac{a}{\sqrt{b}} \frac{l_7^2 \omega_4^2}{l_4} \left(1 + \frac{c^2}{b l_4^2} \right) \tag{8}$$

where

$$\begin{aligned}
a &= \cos^2 \theta_4 \\
b &= 1 - \frac{c^2}{l_4^2} \\
c &= l_5 - l_7 \sin \theta_4
\end{aligned} \tag{9}$$

3.2 Vertical Input from the Slider to the Gripper

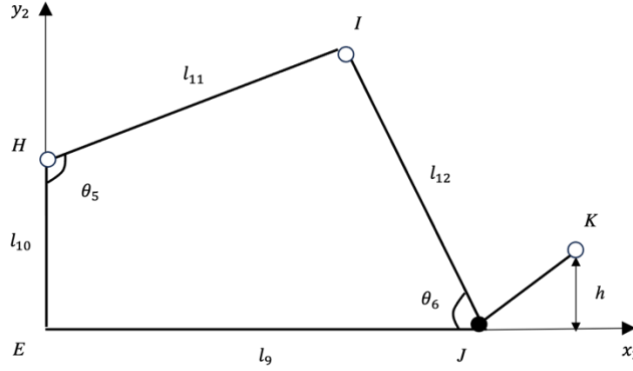


Figure 6. Schematic diagram of the equivalent mechanism of the slider to the vertical input.

In this study, it is assumed that the gripper section receives an input perpendicular to the upper arm through the slider, thereby decoupling the analysis of the gripper from that of the robotic arm. We will now analyze the relationship between the slider and the vertical input to the gripper.

In the four-bar linkage mechanism $EHIJ$ shown in **Figure 6**, segment IJ is perpendicular to JK and remains relatively fixed, while point K slides freely along the vertical black line. HE represents the upper half of the slider. The symbol conventions are illustrated in **Figure 6**. The closed vector equation is formulated as follows:

$$\mathbf{l}_{EH} + \mathbf{l}_{HI} = \mathbf{l}_{EJ} + \mathbf{l}_{JI} \quad (10)$$

By projecting this closed vector equation onto the x and y directions, the position equations are obtained as follows:

$$\begin{aligned} x: \quad 0 + l_{11} \cos(\theta_5 - \frac{\pi}{2}) &= l_9 + l_{12} \cos(\pi - \theta_6) \\ y: \quad l_{10} + l_{11} \sin(\theta_5 - \frac{\pi}{2}) &= 0 + l_{12} \sin(\pi - \theta_6) \end{aligned} \quad (11)$$

These equations form a nonlinear system. Given l_9 , the angles θ_5 and θ_6 can be solved through geometric relationships.

Differentiating yields the velocity relationships:

$$\begin{bmatrix} l_{11} \cos \theta_5 & -l_{12} \sin \theta_6 \\ l_{11} \sin \theta_5 & -l_{12} \cos \theta_6 \end{bmatrix} \begin{bmatrix} \omega_5 \\ \omega_6 \end{bmatrix} = \begin{bmatrix} 1 \\ 0 \end{bmatrix} \frac{dl_9}{dt} \quad (12)$$

Differentiating again provides the acceleration relationships:

$$\begin{bmatrix} l_{11} \cos \theta_5 & -l_{12} \sin \theta_6 \\ l_{11} \sin \theta_5 & -l_{12} \cos \theta_6 \end{bmatrix} \begin{bmatrix} \beta_5 \\ \beta_6 \end{bmatrix} = \begin{bmatrix} 1 \\ 0 \end{bmatrix} \frac{d^2 l_9}{dt^2} - \begin{bmatrix} -l_{11} \omega_5 \sin \theta_5 & -l_{12} \omega_6 \cos \theta_6 \\ l_{11} \omega_5 \cos \theta_5 & l_{12} \omega_6 \sin \theta_6 \end{bmatrix} \begin{bmatrix} \omega_5 \\ \omega_6 \end{bmatrix} \quad (13)$$

From the geometric relationships, θ_6 is related to h as follows:

$$h = l_{13} \tan\left(\frac{\pi}{2} - \theta_6\right) \quad (14)$$

Differentiating yields the velocity relationships:

$$\frac{dh}{dt} = -l_{13}\omega_6(\cot^2 \theta_6 + 1) \quad (15)$$

Differentiating again provides the acceleration relationships:

$$\frac{d^2 h}{dt^2} = 2l_{13}\omega_6^2 \cot^2 \theta_6 (\cot^2 \theta_6 + 1) - l_{13}\beta_6 (\cot^2 \theta_6 + 1) \quad (16)$$

3.3 Vertical Input to the Gripper

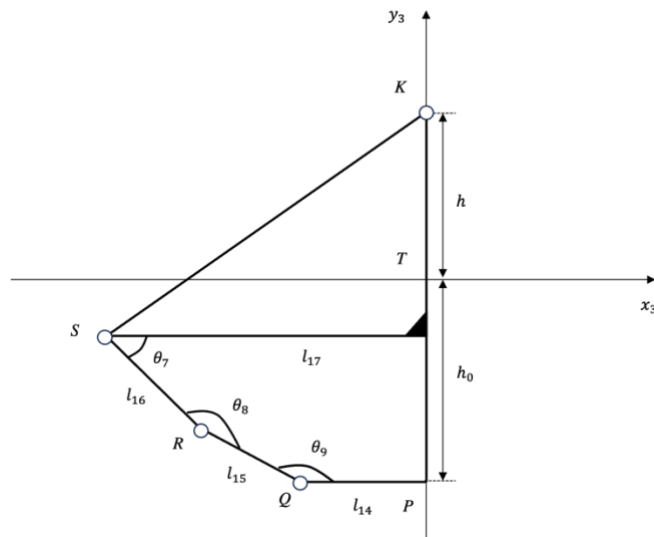


Figure 7. Schematic diagram of the equivalent mechanism of vertical input to the gripper.

The vertical input mechanism is illustrated in **Figure 7**. The horizontal line on which point J is located remains relatively fixed with respect to line PQ , while segment KT always moves along the straight line KP , which is perpendicular to PQ . Other symbol conventions are as shown in the above figure. The closed vector equation is formulated as follows:

$$l_{PO} + l_{OR} = l_{PT} + l_{TS} + l_{SR} \quad (17)$$

By projecting this closed vector equation onto the x and y directions, the position equations are obtained as follows:

$$\begin{aligned} x: & -l_{14} - l_{15} \cos \theta_9 = 0 - l_{17} + l_{16} \cos \theta_7 \\ y: & 0 + l_{15} \sin \theta_9 = h_0 - (l_{KT} - h) + 0 - l_{16} \sin \theta_7 \end{aligned} \quad (18)$$

Differentiating yields the velocity relationships:

$$\begin{bmatrix} l_{16} \sin \theta_7 & l_{15} \sin \theta_9 \\ l_{16} \cos \theta_7 & l_{15} \cos \theta_9 \end{bmatrix} \begin{bmatrix} \omega_7 \\ \omega_9 \end{bmatrix} = \begin{bmatrix} 0 \\ 1 \end{bmatrix} \frac{dh}{dt} \quad (19)$$

Differentiating again provides the acceleration relationships:

$$\begin{bmatrix} l_{16} \sin \theta_7 & l_{15} \sin \theta_9 \\ l_{16} \cos \theta_7 & l_{15} \cos \theta_9 \end{bmatrix} \begin{bmatrix} \beta_7 \\ \beta_9 \end{bmatrix} = \begin{bmatrix} 0 \\ 1 \end{bmatrix} \frac{d^2 h}{dt^2} - \begin{bmatrix} l_{16} \omega_7 \cos \theta_7 & l_{15} \omega_9 \cos \theta_9 \\ -l_{16} \omega_7 \sin \theta_7 & -l_{15} \omega_9 \sin \theta_9 \end{bmatrix} \begin{bmatrix} \omega_7 \\ \omega_9 \end{bmatrix} \quad (20)$$

3.4 Kinematics modeling of Gripper of the Underactuated Metamorphic Loading Manipulator

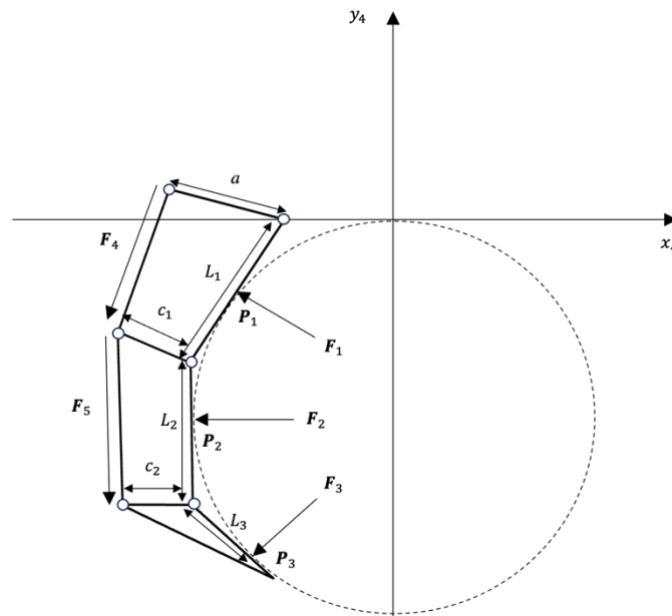


Figure 8. Schematic diagram of the equivalent mechanism of vertical input to the gripper.

In our quest to enhance the design and optimization of the gripper system, we have undertaken a meticulous approach by developing a static model of the gripper's fingers. This model serves as a foundational framework for understanding the mechanical interactions that occur during the grasping process. Our analysis is centered on the contact forces that are pivotal to the gripper's performance, as they directly influence the stability and effectiveness of the grasp.

To streamline the computational process and focus on the core dynamics, we have made certain simplifications. Notably, we have chosen to neglect the gravitational effects acting on the fingers and the frictional forces that arise between the fingers and the object being grasped. This decision is strategic, as it allows us to isolate and analyze the primary forces at play without the added complexity of secondary forces, which can be reintroduced in subsequent stages of the design process for a more comprehensive analysis.

Under the assumption of complete grasping, the contact points are designated as \boldsymbol{P}_1 , \boldsymbol{P}_2 , and \boldsymbol{P}_3 , and their positions can be expressed as follows:

$$\begin{aligned}
\mathbf{P}_1 &= (d_1 \cos \alpha_1, d_1 \sin \alpha_1)^T \\
\mathbf{P}_2 &= (L_1 \cos \alpha_1 + d_2 \cos(\alpha_1 + \alpha_2), L_1 \sin \alpha_1 + d_2 \sin(\alpha_1 + \alpha_2))^T \\
\mathbf{P}_3 &= (L_1 \cos \alpha_1 + L_2 \cos(\alpha_1 + \alpha_2) + d_3 \cos(\alpha_1 + \alpha_2 + \alpha_3), L_1 \sin \alpha_1 + L_2 \sin(\alpha_1 + \alpha_2) + d_3 \sin(\alpha_1 + \alpha_2 + \alpha_3))^T
\end{aligned} \tag{21}$$

Where L_1, L_2, L_3 represent the lengths of the three rods, $\alpha_1, \alpha_1 + \alpha_2, \alpha_1 + \alpha_2 + \alpha_3$ denote the angles between the three structures and the horizontal line, d_1, d_2, d_3 are the distances between the contact points and the joints, $\mathbf{F}_1, \mathbf{F}_2, \mathbf{F}_3$ are the reaction forces of the object.

$$\begin{aligned}
\mathbf{F}_1 &= (F_1 \sin \alpha_1, -F_1 \cos \alpha_1)^T \\
\mathbf{F}_2 &= (F_2 \sin(\alpha_1 + \alpha_2), -F_2 \cos(\alpha_1 + \alpha_2))^T \\
\mathbf{F}_3 &= (F_3 \sin(\alpha_1 + \alpha_2 + \alpha_3), -F_3 \cos(\alpha_1 + \alpha_2 + \alpha_3))^T
\end{aligned} \tag{22}$$

Differentiating the positions of the contact points yields:

$$\begin{aligned}
\dot{\mathbf{P}}_1 &= (-\dot{\alpha}_1 d_1 \sin \alpha_1, \dot{\alpha}_1 d_1 \cos \alpha_1)^T \\
\dot{\mathbf{P}}_2 &= (-\dot{\alpha}_1 L_1 \sin \alpha_1 - d_2 (\dot{\alpha}_1 + \dot{\alpha}_2) \sin(\alpha_1 + \alpha_2), \dot{\alpha}_1 L_1 \cos \alpha_1 + d_2 (\dot{\alpha}_1 + \dot{\alpha}_2) \cos(\alpha_1 + \alpha_2))^T \\
\dot{\mathbf{P}}_3 &= (-\dot{\alpha}_1 L_1 \sin \alpha_1 - L_2 (\dot{\alpha}_1 + \dot{\alpha}_2) \sin(\alpha_1 + \alpha_2) - d_3 (\dot{\alpha}_1 + \dot{\alpha}_2 + \dot{\alpha}_3) \sin(\alpha_1 + \alpha_2 + \alpha_3), \\
&\quad \dot{\alpha}_1 L_1 \cos \alpha_1 + L_2 (\dot{\alpha}_1 + \dot{\alpha}_2) \cos(\alpha_1 + \alpha_2) + d_3 (\dot{\alpha}_1 + \dot{\alpha}_2 + \dot{\alpha}_3) \cos(\alpha_1 + \alpha_2 + \alpha_3))^T
\end{aligned} \tag{23}$$

According to the principle of virtual work, we have:

$$\mathbf{F}_i^T \mathbf{v}_i + \mathbf{M}_i^T \boldsymbol{\omega}_i = 0, i = 1, 2, 3 \tag{24}$$

$$\begin{aligned}
& [\mathbf{F}_1^T \quad \mathbf{F}_2^T \quad \mathbf{F}_3^T]_{1 \times 6} \begin{bmatrix} \dot{\mathbf{P}}_1 \\ \dot{\mathbf{P}}_2 \\ \dot{\mathbf{P}}_3 \end{bmatrix}_{6 \times 1} \\
& = [\mathbf{F}_1^T \quad \mathbf{F}_2^T \quad \mathbf{F}_3^T] \begin{bmatrix} -d_1 \sin(\alpha_1) & 0 & 0 & 0 & 0 & 0 \\ 0 & d_1 \cos(\alpha_1) & 0 & 0 & 0 & 0 \\ -d_1 \sin(\alpha_1) & 0 & -d_2 \sin(\alpha_1 + \alpha_2) & 0 & 0 & 0 \\ 0 & d_1 \cos(\alpha_1) & 0 & d_2 \cos(\alpha_1 + \alpha_2) & 0 & 0 \\ -d_1 \sin(\alpha_1) & 0 & -d_2 \sin(\alpha_1 + \alpha_2) & 0 & -d_3 \sin(\alpha_1 + \alpha_2 + \alpha_3) & 0 \\ 0 & d_1 \cos(\alpha_1) & 0 & d_2 \cos(\alpha_1 + \alpha_2) & 0 & d_3 \cos(\alpha_1 + \alpha_2 + \alpha_3) \end{bmatrix} \begin{bmatrix} \dot{\alpha}_1 \\ \dot{\alpha}_1 \\ \dot{\alpha}_1 + \dot{\alpha}_2 \\ \dot{\alpha}_1 + \dot{\alpha}_2 \\ \dot{\alpha}_1 + \dot{\alpha}_2 + \dot{\alpha}_3 \\ \dot{\alpha}_1 + \dot{\alpha}_2 + \dot{\alpha}_3 \end{bmatrix}
\end{aligned} \tag{25}$$

This leads to the relationship between the torque at the joint and the forces acting at the contact points:

$$\begin{aligned}
F_3 &= \frac{M_3}{d_3} \\
F_2 &= \frac{M_2}{d_2} - \frac{M_3 L_2 \cos \alpha_3}{d_3 d_2} \\
F_1 &= \frac{M_1}{d_1} - \left(\frac{M_2}{d_2} - \frac{M_3 L_2 \cos \alpha_3}{d_3 d_2} \right) \frac{L_1 \cos \alpha_2}{d_1} - \frac{M_3 L_1 \cos(\alpha_2 + \alpha_3)}{d_3 d_1}
\end{aligned} \tag{26}$$

The analysis of the relationship between the forces F_2 and F_1 as a function of the distances between the contact points and the joints d_2 and d_3 is a critical aspect of our study, and this relationship is vividly depicted in **Figures 9** and **10**. These figures provide a visual representation of the dynamic interplay between the forces and the geometry of the gripper system. As illustrated in **Figures 9** and **10**, there is a significant inverse relationship between the contact point distance d_3 and the forces F_1 and F_2 . Specifically, as d_3 increases, F_1 experiences a rapid decrease, while F_2 exhibits a sharp increase. This trend is indicative of the mechanical behavior of the gripper segments in response to the changing contact point positions. In more detail, when the contact point is closer to the end of the gripper, the pressure exerted by the second and third segments on the object increases significantly, which is crucial for securing the object within the gripper. Conversely, the pressure from the first segment diminishes, shifting its role from being a primary force applicator to maintaining the structural integrity of the gripper. This shift aligns perfectly with the gripping process, where the first segment's role is to support the gripper's shape, allowing the second and third segments to apply the necessary pressure for a secure grip.

This observed behavior underscores the rationality and efficacy of the gripper's design. The ability of the gripper to adapt its force distribution based on the contact point positions is a testament to the design's flexibility and responsiveness. It ensures that the gripper can accommodate a variety of object shapes and sizes while maintaining a secure grip, which is a key requirement for applications in robotics and automation.

In conclusion, the analysis presented in **Figures 9** and **10** not only validates the design's theoretical underpinnings but also provides empirical evidence of its practical performance. This insight is invaluable for further refinement of the gripper's design and for informing the development of similar robotic systems that require precise and adaptable gripping capabilities.

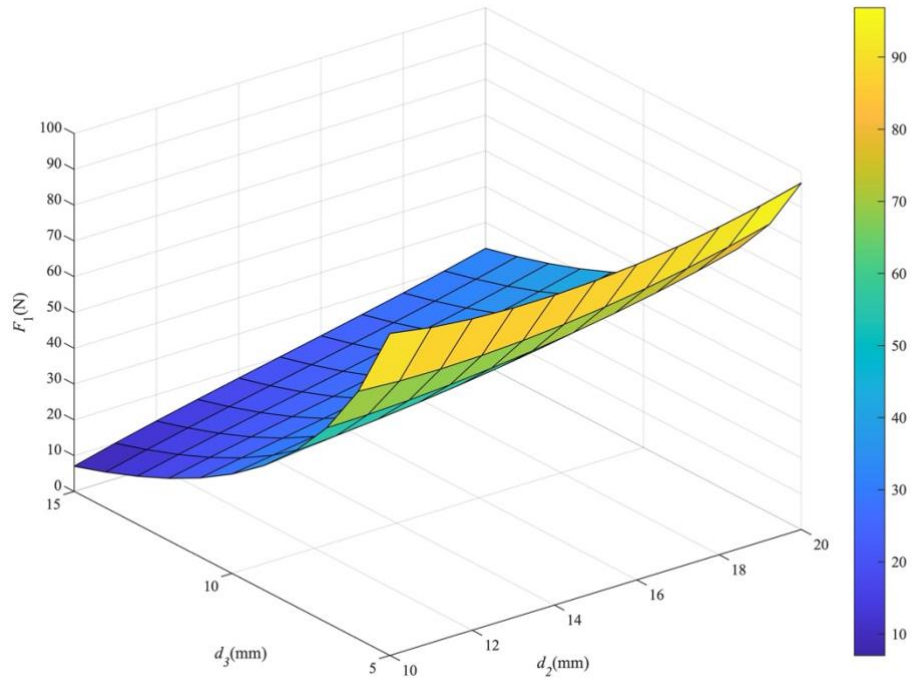


Figure 9. The relationship between F_1 , d_2 and d_3 .

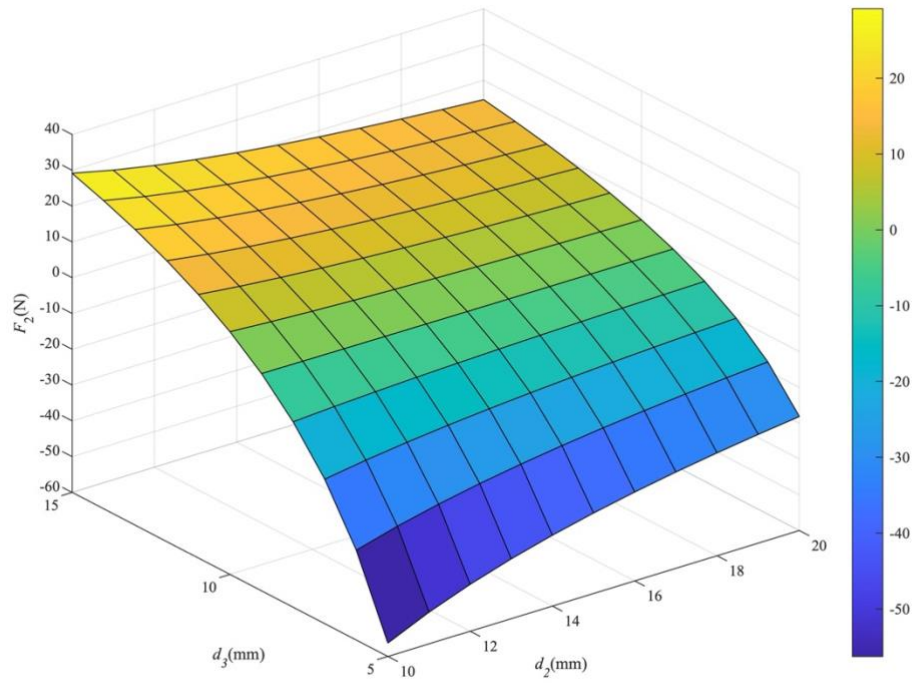


Figure 10. The relationship between F_2 , d_2 and d_3 .

4. Optimization of Gripper Size Parameters

4.1 Formulation of Objective Function

The primary objective of the gripper mechanism is to ensure a reliable and robust grasping function, which is essential for various applications in robotics and automation. This functionality is predicated on the ability to generate sufficient gripping force under the constraints of limited driving power. The challenge lies in striking a delicate balance: the fingers must apply adequate contact forces to securely grasp the object without exerting excessive pressure that could lead to damage. This requirement underscores the need for precision in the design and control of the gripper mechanism.

In an ideal stable grasping scenario, the gripper mechanism must maintain a uniform distribution of contact forces at the finger joints. Uniformity in contact forces is crucial for several reasons. Firstly, it ensures that the object is held securely without any risk of slippage or misalignment. Secondly, it helps to prevent localized stress concentrations that could lead to damage to either the gripper or the object being grasped. Lastly, a uniform force distribution contributes to the longevity and reliability of the gripper mechanism by reducing wear and tear on its components.

In addition to the uniform distribution of forces, the design of the finger mechanism should prioritize compactness and favorable force transmission characteristics. A compact design is not only aesthetically pleasing but also practical, as it allows for the gripper to be integrated into spaces with limited room for maneuver.

Favorable force transmission characteristics are equally important, as they ensure that the forces generated by the driving mechanism are effectively transmitted to the fingers without significant loss or distortion. This efficiency is critical for maximizing the gripper's performance with the available driving power and for ensuring that the gripper can operate effectively across a wide range of grasping scenarios.

In line with these design requirements, the gripper mechanism should be engineered to achieve a uniform distribution of contact forces across all segments.

Let:

$$\begin{aligned} f_{\min} &= \min(F_1, F_2, F_3) \\ f_{\max} &= \max(F_1, F_2, F_3) \end{aligned} \quad (27)$$

Then, the objective function of mechanism parameter optimization is:

$$\Phi(x) = |f_{\min} - f_{\max}| \quad (28)$$

where $x = (a_1, c_1, c_2, k_1, k_2, \tau_1, \tau_2)$.

Assuming the ideal grasping conditions are $\alpha_2 = \alpha_3 = 45^\circ$, the other settings are as follows:

$$\begin{aligned}
L_1 &= 38.3 \text{ mm}, L_2 = 30 \text{ mm}, L_3 = 20.5 \text{ mm} \\
M_1 &= 1000 \text{ N} \cdot \text{mm} \\
F_4 &= \frac{M_1}{a_1} \\
F_5 &= F_4 / \left(\frac{c_2}{c_1}\right) \\
M_2 &= F_4 c_1 - \left(k_1 \frac{\pi}{4} - \tau_1\right) \\
M_3 &= F_5 c_2 - \left(k_2 \frac{\pi}{4} + \tau_2\right)
\end{aligned} \tag{29}$$

Up to this point, we have obtained the objective function and its parameter settings. In the next section, we will carry out optimization using the PSO algorithm based on this objective function.

4.2 Particle Swarm Optimization Algorithm Optimization

The optimization process is a critical component in the design and refinement of complex systems, and in this study, we have leveraged the Particle Swarm Optimization (PSO) algorithm from the MATLAB Optimization Toolbox to achieve our optimization goals. PSO is a powerful computational method that simulates the social behavior of a swarm of particles, where each particle represents a potential solution to the problem at hand. These particles collaboratively explore the search space, adjusting their positions and velocities in response to both their own experiences and the collective intelligence of the swarm.

The PSO algorithm is renowned for its efficacy in tackling complex, nonlinear, and multidimensional optimization challenges. It operates by iteratively refining the solutions, gradually converging towards the global optimum. This is achieved through the interplay of two main components: the personal best solution of each particle, which is the best solution it has encountered, and the global best solution, which is the best solution found by any particle in the swarm.

For our specific application, we have defined the search space boundaries for the optimization parameters. The lower bounds (lb) and upper bounds (ub) for the parameters were set as follows: $lb = [20, 10, 10, 1, 1, -200, -200]$ and $ub = [30, 15, 15, 100, 100, 200, 200]$. These bounds are crucial as they define the limits within which the particles can search for the optimal solution, ensuring that the solutions remain feasible and practical. Assuming the drive torque $M_1 = 1000 \text{ N} \cdot \text{mm}$, the objective function Φ could be obtained through calculation.

To ensure a comprehensive search and to enhance the likelihood of finding a near-optimal solution, we have set the number of particles in the swarm to 1000. This large swarm size allows for a more exhaustive exploration of the search space, increasing the diversity of solutions and reducing the risk of converging prematurely on a suboptimal solution.

Through multiple runs of the PSO algorithm, we have generated a robust set of solutions. A total of 100 distinct solution sets have been identified and are presented in **Figure 11**. These solutions represent the outcomes of our optimization efforts, offering a range of potential configurations that meet the specified criteria and constraints.

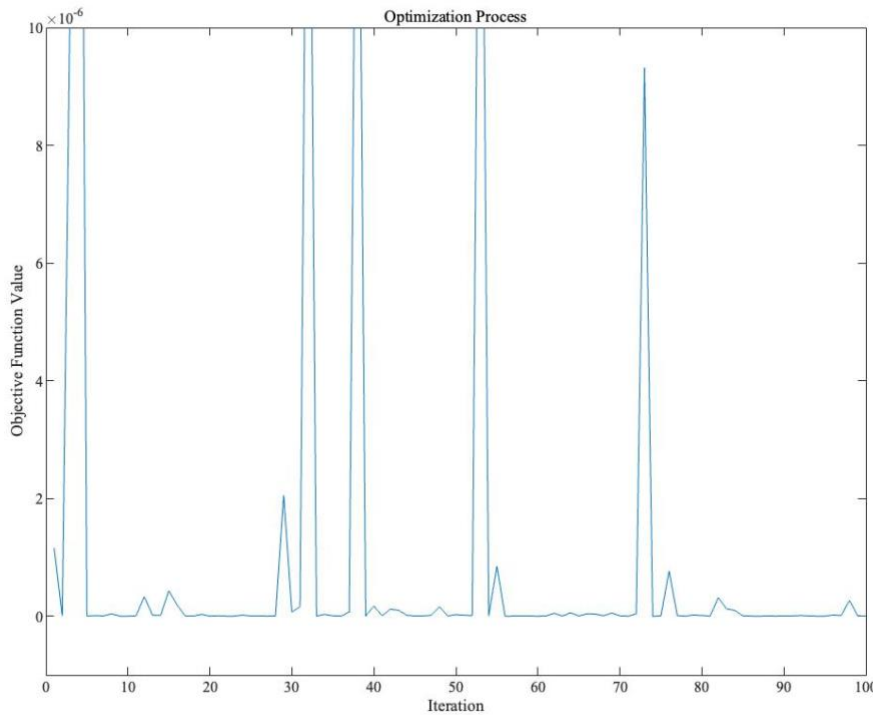


Figure 11. Particle swarm optimization process.

The results from the PSO algorithm not only provide us with a set of optimized parameters but also contribute to a deeper understanding of the underlying relationships and dynamics within the system. By analyzing the solutions presented in **Figure 11**, we can gain insights into the performance of the gripper mechanism under various conditions and make informed decisions to further refine its design.

Comparing the objective function values of the group with the worst performance in parameter optimization and that of the group with the best performance., where:

$$x_a = (26.78, 15.00, 13.35, 34.65, 79.41, -186.56, 199.43)$$

$$x_b = (28.02, 15.00, 13.58, 1.21, 52.56, -184.43, 196.29)$$

The result of objective function shows that Φ_a is 0.0247 and Φ_b is $3.8508 e^{-11}$, which complies with the conditions for the effectiveness of the uniform stress Particle Swarm Optimization process and fulfills the design requirements.

Table 1. Worst and best group parameters of the gripper.

Parameter	Group a	Group b
a_1 (mm)	26.78	28.02
c_1 (mm)	15.00	15.00
c_2 (mm)	13.35	13.58
k_1 (N · mm · rad ⁻¹)	34.65	1.21
k_2 (N · mm · rad ⁻¹)	79.41	52.56
τ_1 (N · mm)	-186.56	-184.43
τ_2 (N · mm)	199.43	196.29
Objective Function Φ	0.0247	$3.8508 e^{-11}$

5. Simulation of Motion and Results

To substantiate the theoretical modeling delineated in this paper, a series of simulations were meticulously executed by grasping different objects using a robot simulation platform on the basis of the mechanism design and structural parameter optimization of the underactuated manipulator.

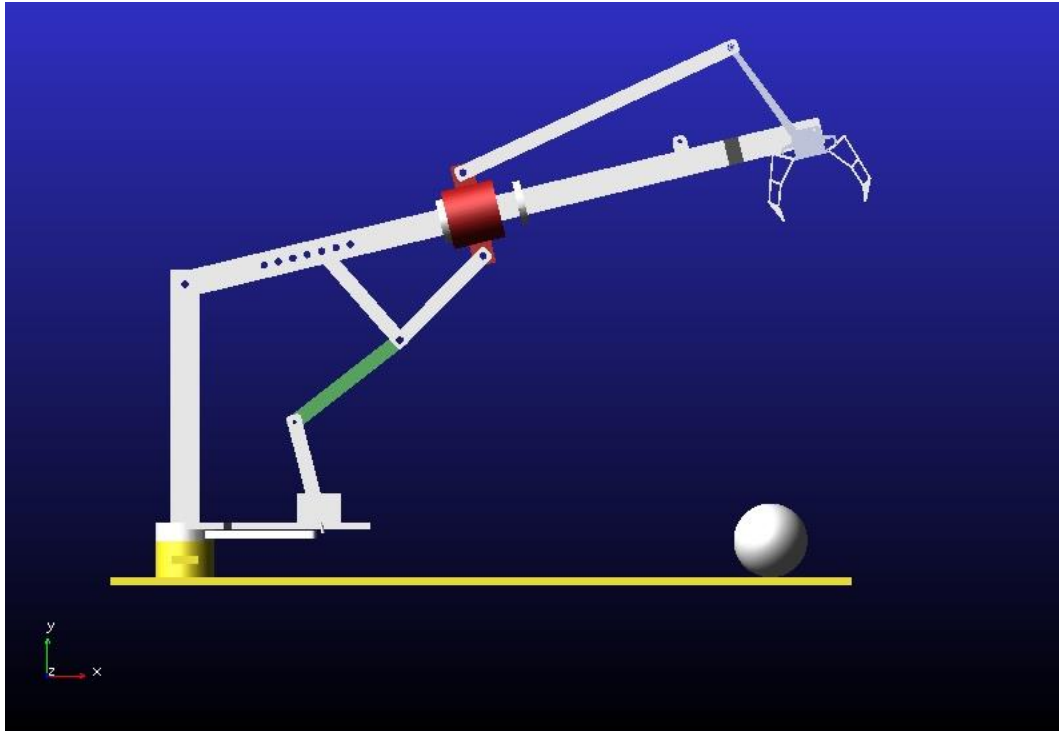


Figure 12. Underactuated metamorphic loading manipulator.

Figure 12 illustrates the 3D simulation model of the underactuated manipulator, which has been engineered in this research, adhering to the principles of metamorphosis. The primary objective of the grasping trials with the underactuated hand was to monitor its performance in securing target objects that fall within a specific volume and mass spectrum. The 3D simulation model of the underactuated manipulator was imported into Adams, where material properties, corresponding kinematic pairs, collision conditions, and actuation information were added to the components.

The primary goal of the grasping trials was to evaluate the manipulator's performance in securing target objects that are defined by a specific volume and mass spectrum. This is a critical test, as it directly assesses the manipulator's ability to handle a variety of objects within its operational parameters, which is essential for its practical application in real-world scenarios.

For the simulations, the 3D simulation model of the underactuated manipulator was imported into Adams, a leading multibody dynamics simulation software. Key simulation parameters included defining material properties to simulate realistic component behavior under various forces, establishing kinematic pairs for accurate motion simulation, and setting collision conditions to prevent unrealistic interactions. These configurations enabled a comprehensive virtual environment that accurately reflects the manipulator's real-world performance. The results of these simulations provide valuable insights into the manipulator's capabilities, limitations, and areas for potential improvement. This validation process is a critical step in the development cycle, ensuring that the proposed design strategies are not only theoretically sound but also practically viable, paving the way for the successful implementation of the underactuated manipulator in various robotic applications.

To accurately assess the manipulative capabilities of the underactuated hand, a focus was placed on manipulating spherical and cylindrical objects, which are frequently encountered in everyday settings. The dc motor used for these tests had a power rating of 12 W. The spherical objects had a diameter of 100 mm and weighted 0.524 kg. While for the cylindrical objects, the base diameter measured 100 mm with a length of 600 mm and weighted 4.94 kg.

When the metamorphic manipulator grabs a spherical object such as a football, the motion trajectory in the simulation platform is shown in **Figure 3**. We can observe that after the grasping action is completed in the 7th second, the contact forces ${}^aF_{L1}$, ${}^aF_{L2}$ and ${}^aF_{L3}$ in parameter group (a) are uneven, which is demonstrated in the simulation vedio attached in Appendix 1. As shown in the experimental results of **Figure 13**, the optimized parameter group (b), after being processed by the PSO algorithm, exhibits a more uniform distribution of the three-finger grasping contact forces ${}^bF_{L1}$, ${}^bF_{L2}$ and ${}^bF_{L3}$ during the grasping process. In contrast, the grasping force of the worst parameter group (a) is more dispersed. This result validates the effectiveness of the PSO algorithm optimization. Furthermore, we can observe that when grasping spherical objects of the same size and weight, the optimized parameter group (b) exerts significantly less three-finger grasping force compared to group (a). This demonstrates that optimized parameters can effectively enhance grasping efficiency and reduce energy consumption.

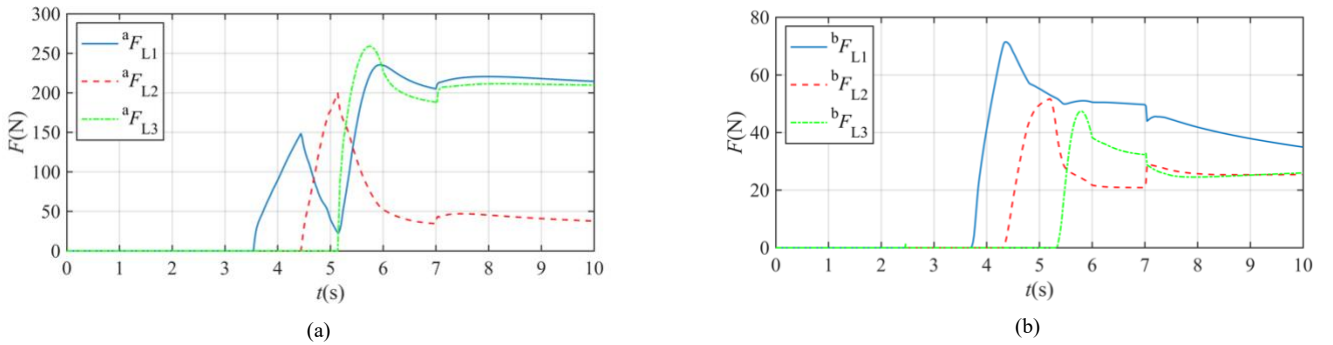


Figure 13. Contact forces of unilateral knuckles when grasping the sphere. (a) Contact forces of unilateral knuckles of the worst group. (b) Contact forces of unilateral knuckles of the best group.

Additionally, the experiment compared the contact forces of the bilateral knuckles during the motion. From **Figure 14**, we can see that the contact forces of the symmetrical bilateral knuckles with the sphere also tend to be uniform in group (b), which verifies the feasibility and optimization of our metamorphic mechanism design and the applicability of the PSO algorithm we used.

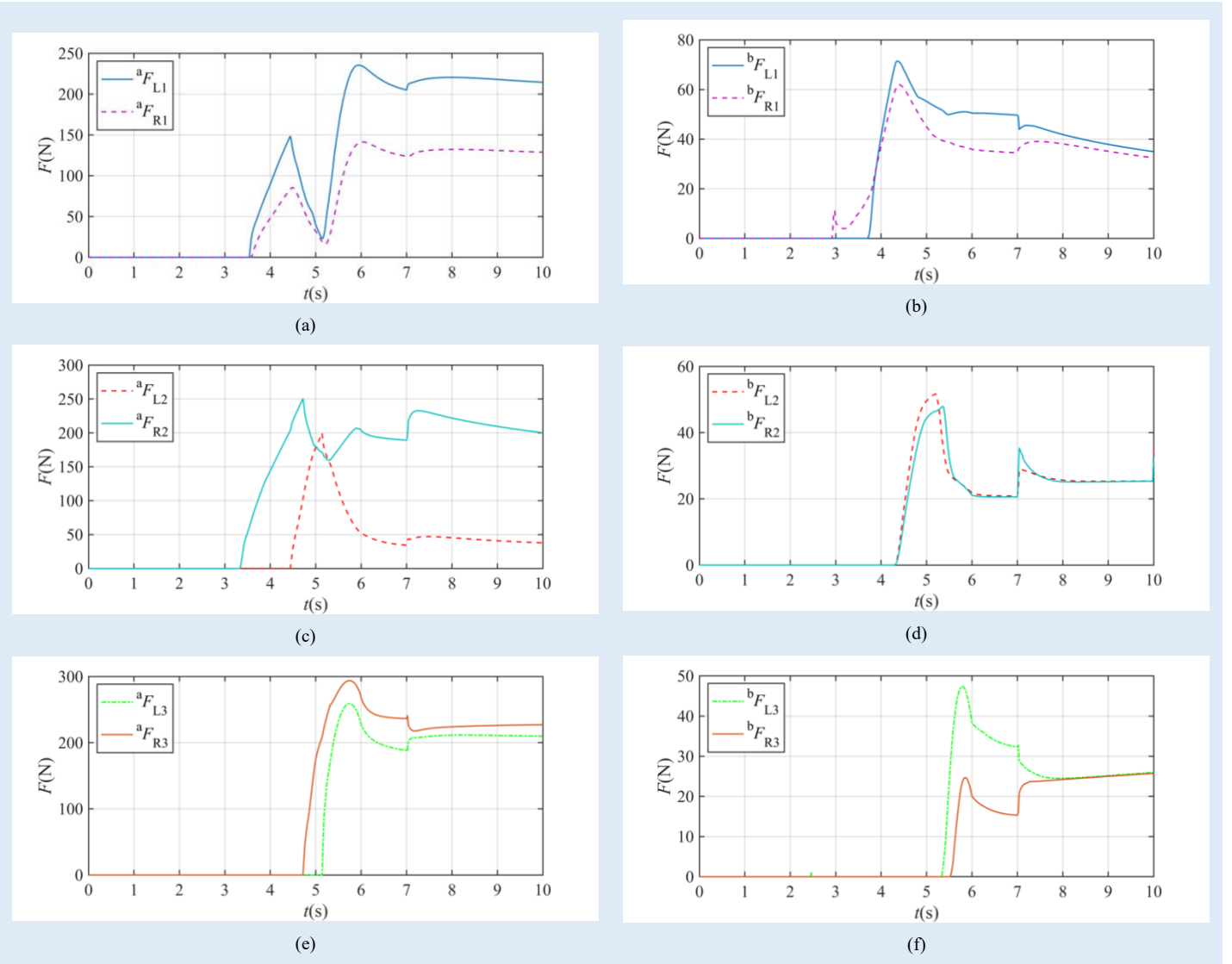


Figure 14. Contact forces of bilateral knuckles during sphere grasping process. (a)-(b) Contact forces 1 of bilateral knuckles of the worst and the best group. (c)-(d) Contact forces 2 of bilateral knuckles of the worst and the best Group. (e)-(f) Contact forces 3 of bilateral knuckles of the worst and the best group.

During the process of enveloping and grasping cylindrical objects such as rebar, the motion trajectory is depicted in **Figure 15**. An important observation regarding the distribution of forces among the knuckles of the metamorphic manipulator can be made from **Figure 15**. It is evident that the force exerted on three knuckles of group (b) is more uniform compared to that on group (a) and the grasping efficiency of group (b) is higher than that of group (a).

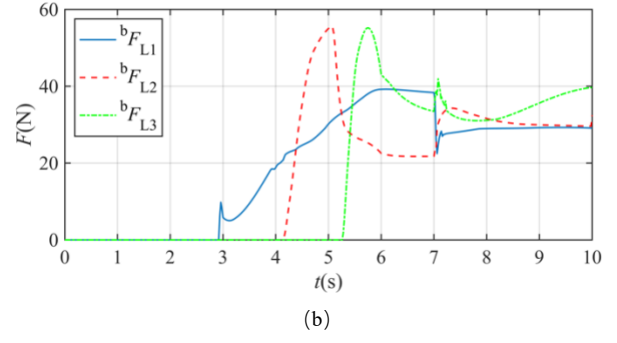
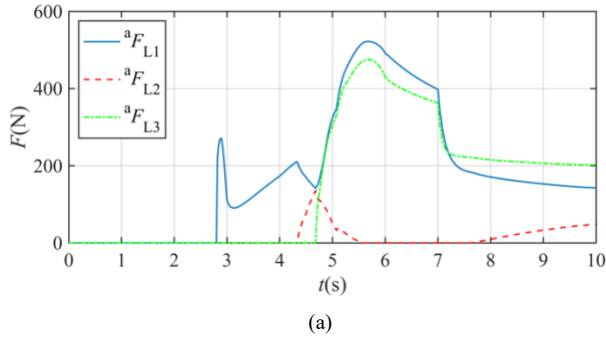
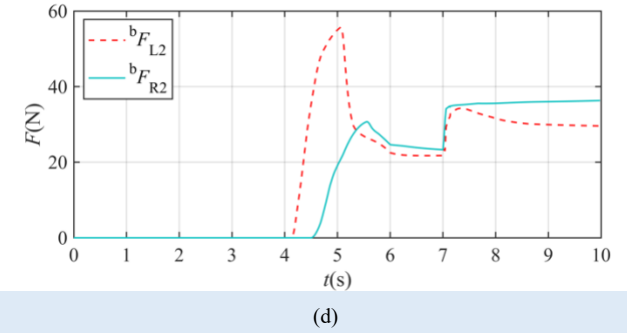
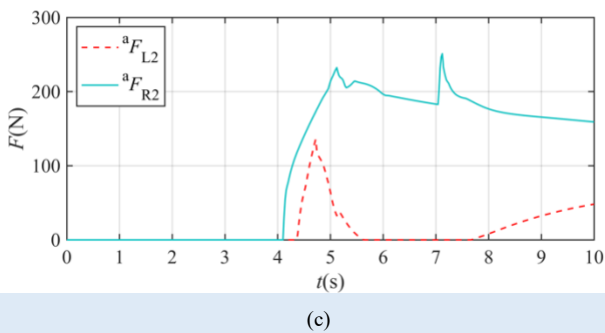
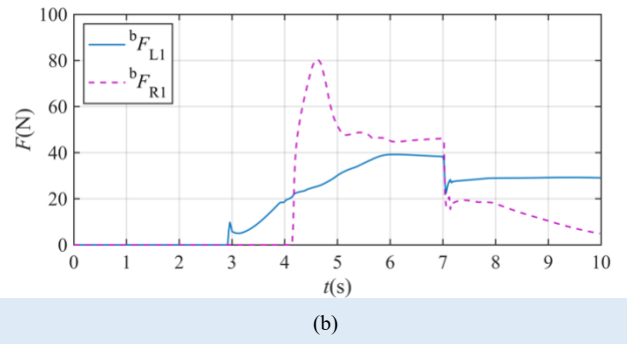
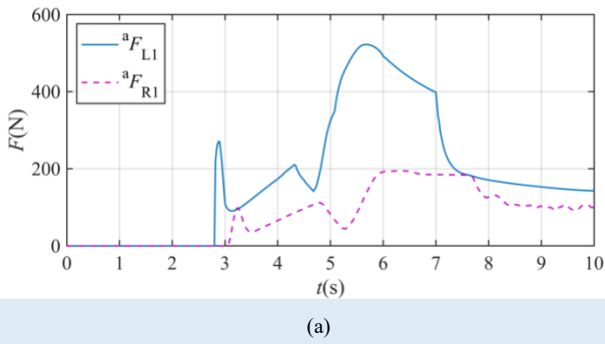


Figure 15. Contact forces of unilateral knuckles when grasping the cylinder. (a) Contact forces of unilateral knuckles of the worst group. (b) Contact forces of unilateral knuckles of the best group.

Furthermore, the experimental analysis was extended to assess the comparative contact forces exerted by the bilateral knuckles throughout the motion sequence. As depicted in **Figure 16**, it is observed that the contact forces at the symmetrical bilateral knuckles with the cylindrical object exhibit a tendency towards uniformity. This observation serves as empirical validation for the efficacy and optimization of the metamorphic mechanism design, as well as the suitability of the Particle Swarm Optimization (PSO) algorithm employed in this study.



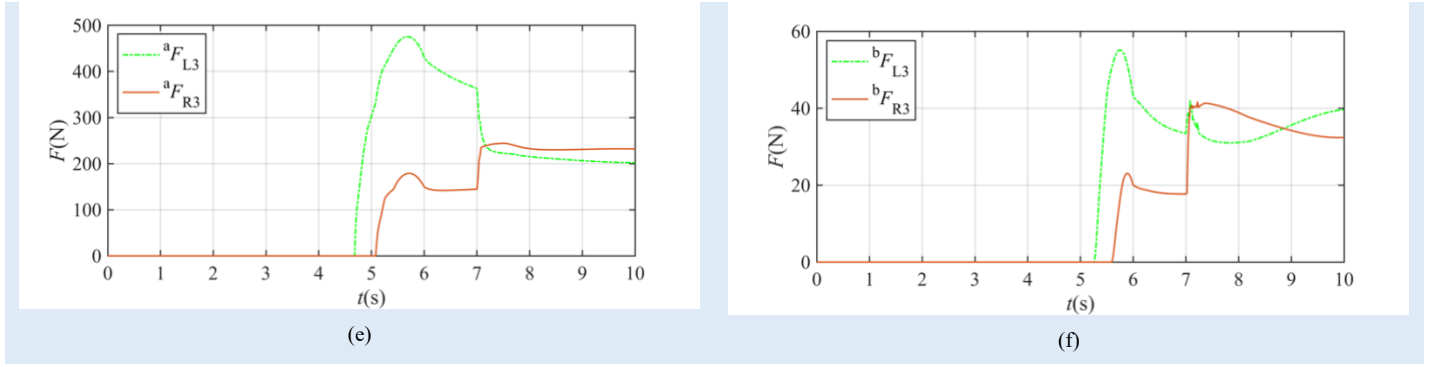


Figure 16. Contact forces of bilateral knuckles during cylinder grasping process. (a)-(b) Contact forces 1 of bilateral knuckles of the worst and the best group. (c)-(d) Contact forces 2 of bilateral knuckles of the worst and the best group. (e)-(f) Contact forces 3 of bilateral knuckles of the worst and the best group.

The simulation experiments conducted with the underactuated hand have yielded promising results, effectively validating the feasibility and stability of the proposed metamorphic mechanism. These experiments have demonstrated the manipulator's capability to adapt to a variety of grasping scenarios, which is a testament to the design's versatility and robustness. By comparing the simulation data results of group (a) and group (b), we can observe that group (b), which is optimized by the PSO algorithm, can achieve stable grasping of objects with a smaller force. This validates the effectiveness of PSO to reduce power consumption.

The simulation results also highlight the manipulator's strength in terms of the maximum grasping force it can exert. When grasping objects, the knuckle was able to apply a force in excess of 500 N for grasping objects. These figures indicate that the manipulator is not only capable of adapting to different objects but also of applying the necessary force to securely grasp and manipulate them. The ability to exert such high forces is a significant indicator of the manipulator's operational capabilities. It suggests that the underactuated manipulator is well-suited for tasks that require a combination of precision and strength, such as in assembly lines, logistics, or any environment where objects need to be moved or manipulated with care and efficiency.

6. Conclusions

This paper introduces a pioneering innovative underactuated metamorphic loading manipulator, showcasing its exceptional grasping force and adaptability across various objects. The kinematic and contact force analyses provide critical insights into the manipulator's real-time structural morphing and interaction dynamics, laying a robust theoretical foundation for design and simulation. To further optimize the performance of the gripper, particle swarm optimization (PSO) has been effectively utilized to refine the size parameters of the gripper's structure. This optimization ensures robust adaptability across various applications, highlighting the manipulator's potential in scenarios that demand efficient and adaptable loading solutions. The simulation validates simplicity, versatility, self-adaptability, and strong grasp ability of the manipulator, with the potential to significantly reduce costs and enhance capabilities in

robotics. The future optimization of this mechanism promises to further enhance its performance in complex environments, solidifying its potential as a versatile tool in industrial automation and unstructured manipulation tasks.

References

1. Wu, P., et al. *Gello: A general, low-cost, and intuitive teleoperation framework for robot manipulators*. in *2024 IEEE/RSJ International Conference on Intelligent Robots and Systems (IROS)*. 2024. IEEE.
2. Townsend, W., *The BarrettHand grasper—programmably flexible part handling and assembly*. Industrial Robot: an international journal, 2000. **27**(3): p. 181-188.
3. Knutti, D., *The Utah/MIT Dexterous Hand: Work in Progrss*. Int'l J. Robotics Research, 1984. **3**(4): p. 21-50.
4. Fukaya, N., et al. *Design of the TUAT/Karlsruhe humanoid hand*. in *Proceedings. 2000 IEEE/RSJ International Conference on Intelligent Robots and Systems (IROS 2000)(Cat. No. 00CH37113)*. 2000. IEEE.
5. Zhou, J., et al., *BCL-13: A 13-DOF soft robotic hand for dexterous grasping and in-hand manipulation*. IEEE Robotics and Automation Letters, 2018. **3**(4): p. 3379-3386.
6. Zhu, J., et al., *Challenges and outlook in robotic manipulation of deformable objects*. IEEE Robotics & Automation Magazine, 2022. **29**(3): p. 67-77.
7. Zhang, W., et al., *Under-actuated humanoid robot hand with end power grasping*. Tsinghua Sci. Technol, 2009. **49**: p. 194-197.
8. Franco, E., et al. *Model based adaptive control for a soft robotic manipulator*. in *2019 IEEE 58th Conference on Decision and Control (CDC)*. 2019. IEEE.
9. She, Y., et al., *Design and Fabrication of a Soft Robotic Hand With Embedded Actuators and Sensors*. Journal of Mechanisms and Robotics, 2015. **7**(2).
10. Laschi, C., et al., *Soft Robot Arm Inspired by the Octopus*. Advanced Robotics, 2012. **26**(7): p. 709-727.
11. Wang, Z., Y. Torigoe, and S. Hirai, *A prestressed soft gripper: design, modeling, fabrication, and tests for food handling*. IEEE Robotics and Automation Letters, 2017. **2**(4): p. 1909-1916.
12. Wei, S.J.W., T.Y.; Gu, G.Y., *Design of a soft pneumatic robotic gripper based on fiber-reinforced actuator*. Journal of Mechanical Engineering, 2017. **53**(13): p. 29-38.
13. Hao, Y., et al., *Modeling and experiments of a soft robotic gripper in amphibious environments*. International Journal of Advanced Robotic Systems, 2017. **14**(3): p. 1729881417707148.
14. Liu, C.-H., et al., *Optimal design of a soft robotic gripper for grasping unknown objects*. Soft robotics, 2018. **5**(4): p. 452-465.
15. Ghodsian, N., et al., *Mobile manipulators in Industry 4.0: A review of developments for industrial applications*. Sensors, 2023. **23**(19): p. 8026.
16. He, B., S. Wang, and Y. Liu, *Underactuated robotics: a review*. International Journal of Advanced Robotic Systems, 2019. **16**(4): p. 1729881419862164.
17. Dollar, A.M. and R.D. Howe, *The highly adaptive SDM hand: Design and performance evaluation*. The international journal of robotics research, 2010. **29**(5): p. 585-597.
18. Liang, D. and W. Zhang, *PASA-GB Hand: a novel parallel and self-adaptive robot hand with gear-belt mechanisms*. Journal of Intelligent & Robotic Systems, 2018. **90**: p. 3-17.
19. Begoc, V., et al. *Mechanical design of a new pneumatically driven underactuated hand*. in *Proceedings 2007 IEEE International Conference on Robotics and Automation*. 2007. IEEE.

20. Birglen, L. and C.M. Gosselin. *On the force capability of underactuated fingers*. in *2003 IEEE International Conference on Robotics and Automation (Cat. No. 03CH37422)*. 2003. IEEE.
21. Birglen, L. and C.M. Gosselin, *Grasp-state plane analysis of two-phalanx underactuated fingers*. Mechanism and Machine Theory, 2006. **41**(7): p. 807-822.
22. Gosselin, C.M., *Adaptive Robotic Mechanical Systems: A Design Paradigm*. Journal of Mechanical Design, 2005. **128**(1): p. 192-198.
23. Moosavian, A. and F.J. Xi, *Holonomic under-actuation of parallel robots with topological reconfiguration*. Mechanism and Machine Theory, 2016. **96**: p. 290-307.
24. Li, X., et al., *The effect of different denitrification and partial nitrification-Anammox coupling forms on nitrogen removal from mature landfill leachate at the pilot-scale*. Bioresource Technology, 2020. **297**: p. 122430.
25. Gao, C., et al., *Dynamic analysis of a three-fingered deployable metamorphic robotic grasper*. Mechanism and Machine Theory, 2023. **180**: p. 105140.
26. Wang, L., et al., *A control strategy based on trajectory planning and optimization for two-link underactuated manipulators in vertical plane*. IEEE Transactions on Systems, Man, and Cybernetics: Systems, 2021. **52**(6): p. 3466-3475.
27. Wei, G., et al., *Kinematic analysis and prototype of a metamorphic anthropomorphic hand with a reconfigurable palm*. International Journal of Humanoid Robotics, 2011. **8**(03): p. 459-479.
28. Dai, J.S. and D. Wang, *Geometric Analysis and Synthesis of the Metamorphic Robotic Hand*. Journal of Mechanical Design, 2006. **129**(11): p. 1191-1197.
29. Tang, Z., et al., *Origaker: a novel multi-mimicry quadruped robot based on a metamorphic mechanism*. Journal of Mechanisms and Robotics, 2022. **14**(6): p. 060907.
30. Dai, J.S., Ding, X., & Zou, H. J., *Fundamentals and categorization of metamorphic mechanisms*. Journal of Mechanical Engineering, 2005. **41**(6): p. 7-12.
31. Wang, R., X. Kang, and J.S. Dai, *A novel reconfigurable spherical joint based on linear independence of screws and its resultant metamorphic mechanisms*. Mechanism and Machine Theory, 2021. **164**: p. 104351.
32. Wang, Z., W. Zhang, and X. Ding, *Design and analysis of a novel metamorphic remote-centre-of-motion mechanism with parallelogram joints*. Mechanism and Machine Theory, 2022. **176**: p. 105038.
33. Gao, C., et al., *Design and analysis of a novel truss-shaped variable-stiffness deployable robotic grasper*. IEEE access, 2020. **8**: p. 112944-112956.
34. Wang, D., & Dai, J. S., *Theoretical foundation of metamorphic mechanism and its synthesis*. Journal of Mechanical Engineering, 2007. **43**(8): p. 32-42.
35. Dai, J.S. and J.R. Jones. *Mobility in Metamorphic Mechanisms of Foldable/Erectable Kinds*. in *ASME 1998 Design Engineering Technical Conferences*. 1998.
36. Dai, J.S., Z. Huang, and H. Lipkin, *Mobility of Overconstrained Parallel Mechanisms*. Journal of Mechanical Design, 2004. **128**(1): p. 220-229.
37. Kuo, C.-H., J.S. Dai, and H.-S. Yan. *Reconfiguration principles and strategies for reconfigurable mechanisms*. in *2009 ASME/IFTOMM International Conference on Reconfigurable Mechanisms and Robots*. 2009. IEEE.
38. Rodriguez Leal, E. and J.S. Dai. *From origami to a new class of centralized 3-DOF parallel mechanisms*. in *International Design Engineering Technical Conferences and Computers and Information in Engineering Conference*. 2007.
39. Aimedee, F., et al., *Systematization of morphing in reconfigurable mechanisms*. Mechanism and machine theory, 2016. **96**: p. 215-224.
40. Zhang, L., D. Wang, and J.S. Dai, *Biological Modeling and Evolution Based Synthesis of Metamorphic Mechanisms*. Journal of Mechanical Design, 2008. **130**(7).
41. Yan, H.-S. and C.-H. Kuo, *Topological Representations and Characteristics of Variable Kinematic Joints*. Journal of Mechanical Design, 2005. **128**(2): p. 384-391.

42. Wohlhart, K. *Multifunctional 7R linkages*. in *Proceedings of the International Symposium on Mechanisms and Machine Theory, AzCIFTToMM, Izmir, Turkey*. 2010.
43. Wang, R., Y. Song, and J.S. Dai, *Reconfigurability of the origami-inspired integrated 8R kinematotropic metamorphic mechanism and its evolved 6R and 4R mechanisms*. *Mechanism and Machine Theory*, 2021. **161**: p. 104245.
44. Abdelmaksoud, S.I., et al., *In-Depth Review of Advanced Control Strategies and Cutting-Edge Trends in Robot Manipulators: Analyzing the Latest Developments and Techniques*. IEEE Access, 2024.
45. Dai, J.S., D. Wang, and L. Cui, *Orientation and workspace analysis of the multifingered metamorphic hand—Metahand*. *IEEE Transactions on Robotics*, 2009. **25**(4): p. 942-947.
46. Shami, T.M., et al., *Particle swarm optimization: A comprehensive survey*. *Ieee Access*, 2022. **10**: p. 10031-10061.
47. Yang, X.-S., *Nature-inspired optimization algorithms: Challenges and open problems*. *Journal of Computational Science*, 2020. **46**: p. 101104.
48. Liang, Y., et al., *Mechanism design and optimization of a haptic master manipulator for laparoscopic surgical robots*. *IEEE Access*, 2019. **7**: p. 147808-147824.
49. Luh, G.-C., C.-Y. Lin, and Y.-S. Lin, *A binary particle swarm optimization for continuum structural topology optimization*. *Applied Soft Computing*, 2011. **11**(2): p. 2833-2844.
50. Jain, M., et al., *An overview of variants and advancements of PSO algorithm*. *Applied Sciences*, 2022. **12**(17): p. 8392.
51. Zhang, J., et al., *Moving-distance-minimized PSO for mobile robot swarm*. *IEEE Transactions on Cybernetics*, 2021. **52**(9): p. 9871-9881.
52. Gong, C., Y. Sun, and L. Yuan, *Study on application of hybrid optimization algorithm in parameters optimization of manipulator*. *Journal of System Simulation*, 2019. **30**(1): p. 105-113.
53. Wang, W., et al., *A universal index and an improved PSO algorithm for optimal pose selection in kinematic calibration of a novel surgical robot*. *Robotics and computer-integrated manufacturing*, 2018. **50**: p. 90-101.
54. L. Fang, P.D., *Kinematic calibration method of robots based on quantum-behaved particle swarm optimization*. *Journal of Mechanical Engineering*, 2016. **52**(7): p. 23-30.
55. Gao, G., et al., *Hybrid Optimal Kinematic Parameter Identification for an Industrial Robot Based on BPNN-PSO*. *Complexity*, 2018. **2018**(1): p. 4258676.